Linking glass-transition behaviour to photophysical and charge transport properties of high-mobility conjugated polymers

Mingfei Xiao[1], Aditya Sadhanala[1], Mojtaba Abdi-Jalebi[1], Tudor H. Thomas[1], Xinglong Ren[1], Tao Zhang[3], Hu Chen[2], Remington L. Carey[1], Qijing Wang[1], Satyaprasad P. Senanayak[1], Cameron Jellett[4], Ada Onwubiko[4], Maximilian Moser[4], Hailiang Liao[5], Wan Yue[5], Iain McCulloch[2,4], Mark Nikolka[1]*, Henning Sirringhaus[1]*

1. Optoelectronics Group, Cavendish Laboratory, JJ Thomson Avenue, Cambridge, CB3 0HE, UK.
2. KSC, King Abdullah University of Science and Technology (KAUST), Thuwal, 23955-6900, Saudi Arabia.
3. Center for Advancing Electronics Dresden, Technical University Dresden, 01062 Dresden, Germany
4. Department of Chemistry, Imperial College London, South Kensington, SW7 2AZ, UK.
5. Key Laboratory for Polymeric Composite and Functional Materials of Ministry of Education, School of Materials Science and Engineering, Sun Yat-Sen University, Guangzhou, 510275, China.

Abstract

The measurement of the mechanical properties of conjugated polymers can reveal highly relevant information linking optoelectronic properties to underlying microstructures and the knowledge of the glass transition temperature (T_g) is paramount for informing the choice of processing conditions and for interpreting the thermal stability of devices. In this work, we use dynamical mechanical analysis (DMA) to determine T_g of a range of state-of-the-art conjugated polymers with different degrees of crystallinity that are widely studied for applications in organic field-effect transistors (OFETs). We compare our measured values for T_g to the theoretical value predicted by a recent work based on the concept of effective mobility ζ. The comparison shows that for conjugated polymers with a modest length of the monomer units, the T_g values agree well with theoretical predictions. However, for the near-amorphous, indacenodithiophene–benzothiadiazole (IDT-BT) family of polymers with more extended backbone units, values for T_g appear to be significantly higher predicted by theory. We find instead that values for T_g are correlated with the sub-bandgap optical absorption suggesting the possible role of the interchain short contacts within materials' amorphous domains.

Introduction

Due to their compatibility with low-temperature solution processing, conjugated polymers are considered promising candidates for applications in large-area printable electronics, optoelectronics, and bioelectronics[1][2][3][4][5][6][7][8][9][10][11][12][13][14][15][16][17][18][19][20][21][22][23]. Owing to this wealth of potential applications, there has been a long-standing interest in understanding the structure-property relationships of a wide range of conjugated polymers including their charge transport [24][25][26][27][28][29][30] and photophysical properties [31]. Concomitantly, the emerging interest in applications such as electronic skin, that require a high level of flexibility and stretchability,[32] makes it increasingly important to complement these advancements with a detailed understanding of the mechanical properties of these van der Waals bonded, disordered materials. Given that physical parameters, such as the elastic modulus, entanglement molecular weight, glass transition and melting temperatures, are important factors that determine structure-processing-property relationships, there have been growing efforts to correlate the mechanical properties of conjugated polymers and understand them in terms of the underpinning microstructure [33][34] .

The glass transition temperature, T_g, is the temperature at which the amorphous regions change from a glassy to a rubbery state reflecting the elevated mobility of individual polymer chains at higher temperatures[34][35][36][37]. It is not a well-defined, thermodynamic phase transition but depends on experimental conditions; it is related to the temperature at which the timescale for the temperature-dependent structural relaxation of the polymer becomes comparable to the timescale of the experiment. Even for the most crystalline conjugated polymers, solution-processed thin films tend to have a mixed microstructure composed of crystalline and amorphous domains[27]. Their relative proportions depend on the chemical design of the polymer [38] and processing conditions[39]. Investigation of glass transition behavior is hence relevant for all thin films of conjugated polymers. The glass transition process is sometimes referred to as the α-transition or relaxation, which is the main relaxation process for conjugated polymers and involves substantial coordinated backbone motion (including translational and rotational motion [40]). It is associated with a clear change in the materials' mechanical properties. There exist other relaxation processes for conjugated polymers as well, which occur typically at lower temperatures, namely the γ-and β-transitions with $T_\gamma \leqslant T_\beta \leqslant T_g$ [41]. The associated relaxation processes involve smaller energy scales and structural relaxation over more localized length scales. More specifically, the γ-transition with

the lowest temperature corresponds to the activation of highly localized motion or bond deformation such as stretching and bending[42], while at higher temperatures, T_β, larger-scale segment motion involving whole molecular units, such as the solubilizing side chains, are expected to set in[41]. At temperatures above T_g, the melting temperature T_m is reached and the polymer chains within both amorphous and crystalline domains slide freely[35].

In the literature, T_g has been used to quantify mechanical[43] and thermal properties[35][44] of an extensive library of materials used in a variety of electronic and optoelectronic devices. Knowing the T_g of conjugated polymers not only has practical implications for polymer processing like predicting morphological stability of materials[45][46][47] and optimizing annealing protocols[35] of films but also gives information about the polymers' basic properties at molecular levels, such as the backbone rigidity and interchain interaction [35] . Stiffer backbones tend to induce higher T_g, due to a higher barrier to translational and rotational motion. Thus, T_g has been well correlated with persistence length[48] and rotational volume[49][50] for different conjugated polymers. Taking a step further, Gomez *et al.* recently proposed an elegant theoretical model to predict T_g based on information merely from the chemical structure of the repeating units: an effective molecular mobility value, ζ, is proposed to parameterise the rigidity of polymers' repeating units and, thereby, T_g, is predicted by the equation:

$$T_g = 979\text{-}1102\ \zeta\ ℃ \quad (1)$$

while the value of ζ is in turn determined from an average of atomic mobility values assigned to the individual functional groups of the polymer chains.[51]

There is a need for improved, experimental techniques that are able to detect with sufficient sensitivity the glass transition of thin polymer films. Here, we use dynamic mechanical analysis (DMA) to detect the β and α transitions of a wide range of conjugated polymers. DMA is one of the most sensitive experimental techniques for detecting glass transitions and structural relaxation processes. It involves applying an oscillating strain $\gamma^* = \gamma_0 \cdot exp\,(i\omega t)$ with amplitude γ_0 and oscillation frequency ω to a sample of the polymer powder and measuring the resulting stress $\sigma^* = \sigma_0 \cdot exp\,[i(\omega t + \delta)]$ with amplitude σ_0 and a phase delay δ between the stress and strain. This allows determination of the complex modulus $G^* = G' + i \cdot G'' = \frac{\sigma^*}{\gamma^*}$ where $G' = \frac{\sigma_0}{\gamma_0} \cdot cos\,\delta$ is the storage modulus and $G'' = \frac{\sigma_0}{\gamma_0} \cdot sin\,\delta$ is the loss modulus. A plot of the damping factor $tan\,\delta = \frac{G''}{G'}$ gives information about the viscoelastic

property of samples as a function of temperature and frequency. As a general trend, polymers lose elasticity (decrease of storage modulus) and gain viscosity (an increase of loss modulus) during β or α transition, resulting in a peak of the damping factor, which allows locating the related transition temperature. Compared with other commonly used methods to measure T_g, such as differential scanning calorimetry (DSC) [52][53], which is based on the measurements of variations in the polymer's heat capacity, DMA could demonstrate several orders of magnitude higher sensitivity to the detection of the glass transition[54], since it captures the large, associated changes of mechanical properties directly. Therefore, the application of DMA to conjugated polymers offers unique insight into the properties of the amorphous regions in these high mobility polymers and advances our understanding of the relationship between the chemical design of the polymers and the microstructures of the amorphous domains that cannot be obtained from X-ray diffraction experiments. This is important since we can begin to link the elusive amorphous regions in these state-of-the-art conjugated polymers to the observed photophysical and charge transport properties.

In this study we compare a family of conjugated polymers that have been of particular interest for applications in organic field-effect transistors (OFETs): We include polyalkylthiophene polymers, such as poly(3-hexylthiophene) (P3HT), and two polydialkylfluorene polymers, poly (9,9-dioctylfluorene-*alt*-benzothiadiazole) (F8BT) and poly (9,9-dioctylfluorene-*alt*-bithiophene) (F8T2) (Figure 1a) and compare our results to recent near-amorphous, high-mobility and low disorder polymer derivatives from the IDT-BT family of materials (Figure 1b). These polymers are amongst the highest performing polymer semiconductors discovered to date allowing insight into the interplay between mechanical and electrical properties. In polymers like IDT-BT a near-planar, highly rigid backbone[24][55] allows charges to delocalize over long distances along the polymer backbone. Some close-contact points/aggregate regions or crystallites are needed to ensure effective interchain transport. In recent years, efforts have been made to optimise the performance of these materials [56], and to understand the microscopic interactions between chains [31], but a full understanding of the role of the amorphous domains in charge transport remains elusive. An important aim of the present study is to report the glass transition temperature of these polymers, which to the best of our knowledge, have not been studied yet. This is important because a knowledge of the temperature at which mechanical relaxation processes and glass transitions occur is generally needed to inform process conditions for obtaining desired microstructures as well as for understanding the thermal stability of devices. More importantly,

by comparing the experimental and theoretical T_g values allows correlating backbone rigidity to the nature of the relaxation behavior. Lastly, a series of highly crystalline conjugated polymers are measured as well (Figure 1c). Unfortunately, unambiguous backbone glass transition signals are difficult to detect in these system due to the small portion of amorphous regions, which agrees well with the recent results presented by Andersson *et al* [57].

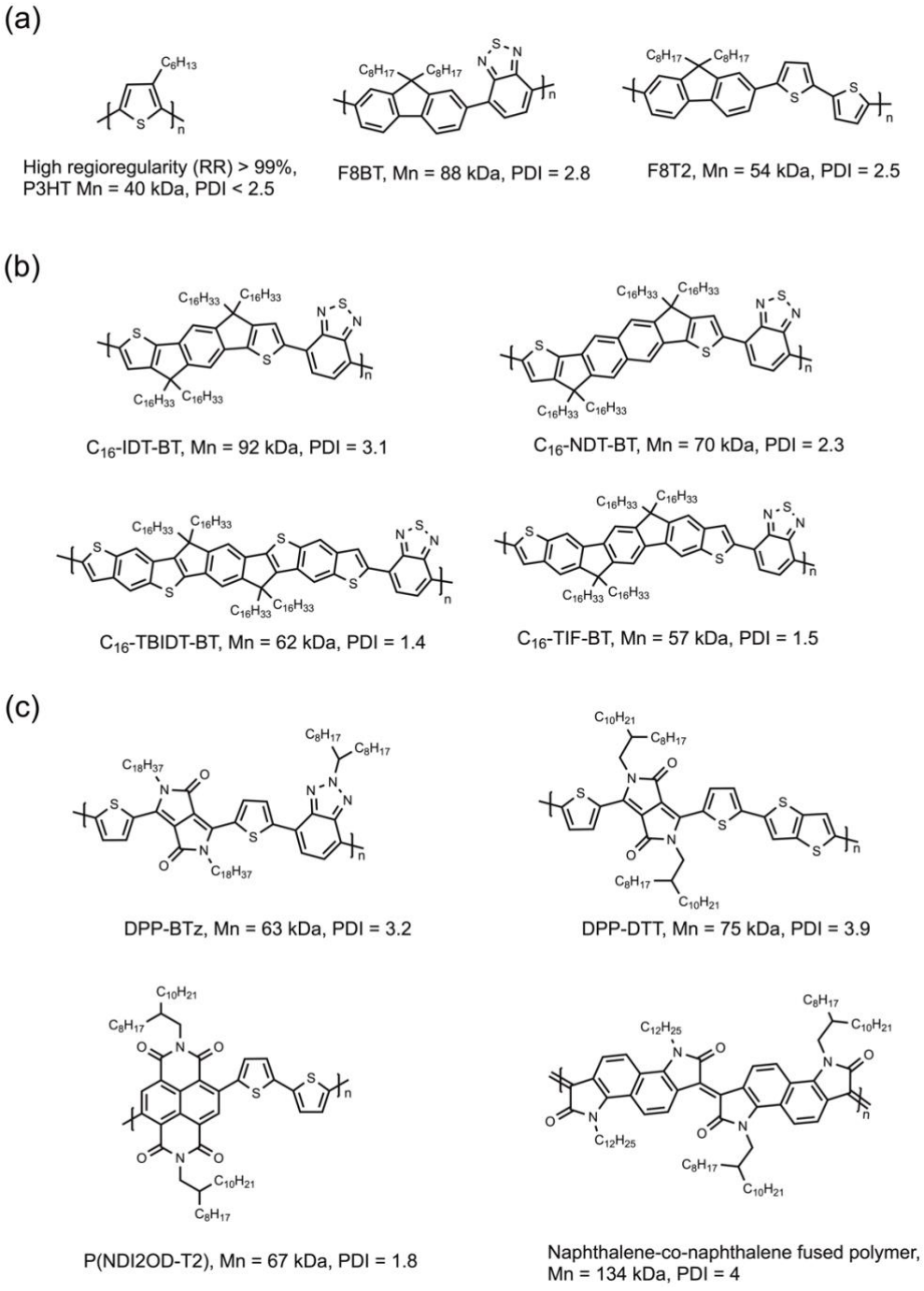

Figure 1 Chemical structures and molecular weight information of polymers used in this work

Results

Temperature-dependent DMA results reveal materials' thermodynamic properties, including the storage modulus, the loss modulus, and the damping factor tan (δ). Stainless steel material pockets[58] were used to envelop the polymer powder so that it could be clamped to the sample holder and drive shaft of the setup for the shearing process during characterisation. This allows measurements of relatively small amounts of polymer powder (7.5 mg) enclosed in the steel pocket. We first present temperature-dependent DMA results for P3HT, F8BT and F8T2 with modulus (solid circles) and tan (δ) (open circles) of material pocket enveloped (MPE) samples characterised with two oscillating frequencies of 1 Hz (red curves) and 10 Hz (blue curves), respectively. In Figure 2 (a), (c), and (d), *G'* (solid circles) and tan (δ) (open circles) of the three polymers are presented. For all the three polymers, *G'* shows a monotonic decrease during the temperature increase, while for tan (δ), specific peaks exist, the position of which indicates the β-transition, α-transition, and the melting process of the materials investigated.

More specifically, for regioregular (RR) P3HT, three distinct transitions manifesting themselves as peaks of the damping factor within the measured temperature range between -150 °C and 300 °C are observed (Figure 2(a)): A first transition is observed at -90 °C for the 1Hz modulation frequency and at -83°C for the 10 Hz modulation frequency. We interpret this as the β-transition associated with the side chain relaxation process. The second transition at 28 °C (35 °C) for the 1(10) Hz modulation is interpreted as the α-transition/glass transition associated with the backbone relaxation. The melting transition is observed at 251 °C and is independent of modulation frequency.

Interestingly, for both β- and α-transitions, higher frequency measurements lead to higher temperature peaks in the damping factor, while for the melting process, such frequency dependence is absent. This agrees well with the nature of the glass transition as a relaxation process, as explained above [59] : at a faster modulation frequency, a higher temperature is needed for the timescale of relaxation to match the timescale of the experiment. In contrast, the melting process is a time-independent first-order phase transition for which no frequency dependence is expected. We note that the value of the storage modulus obtained in the experiment is dominated by the steel pocket that holds the polymer material and can't be directly interpreted. For example, the storage modulus for the MPE samples is in between the value of pure RR P3HT [60] and the value of the stainless steel [61] (Figure 2(b)). However, the

peaks of tan (δ) can be interpreted as transition purely related to the polymer, as steel does not exhibit any detectable relaxation processes in this temperature range.

For the two polydialkylfluorene polymers F8BT and F8T2 the β-, α-transitions, and the melting process are also shown clearly in the DMA measurements. These two polymers show a much weaker β-transition than RR P3HT, both at around -30 °C. However, prominent α-transitions are observed for these two polymers: For F8BT, the transition happens at 100 °C (1 Hz) and 107 °C (10 Hz), while for F8T2, the transition happens at around 113 °C for both 1 Hz and 10 Hz modulation. The melting process at higher temperatures could also be observed from the damping factor.

These results demonstrate clearly that the DMA technique, together with the material pocket accessory, is sufficiently sensitive to accurately and unambiguously capture the nature of β- and α-transitions together with the melting process in these three conjugated polymers. Since the glass transition process is a frequency-dependent relaxation process, hereafter we would mostly focus on the discussion of the lower frequency, namely the 1 Hz results to make our DMA results comparable to the results characterised by other techniques, for example, the shear rheometry (oscillation frequency of 1 rad/s) technique used in the recent work by Gomez *et al.* [51]. More specifically, we compare the T_g values of these three polymers probed from our 1 Hz DMA measurements (at the related peaks in tan (δ)) to the theoretical values predicted by equation (1) and oscillatory shear rheometry measurement results[51], results of which summarised in Table 1. The comparison clearly shows that the T_g measured from DMA agrees well with the theoretically predicted value and the measured value from oscillatory shear rheometry presented in ref. [51], which validates the use of DMA for locating the β-transition, α-transition and the melting process of the materials investigated. The electronic properties of these materials have been studied over many years, however with charge carrier mobilities on the order of 0.1 $cm^2 V^{-1}s^{-1}$ [62][63][64] , their performances are significantly lower than that of the state-of-the-art donor-acceptor polymer families that exceed mobilities of 1 $cm^2 V^{-1}s^{-1}$ [65] on which we will focus now [66].

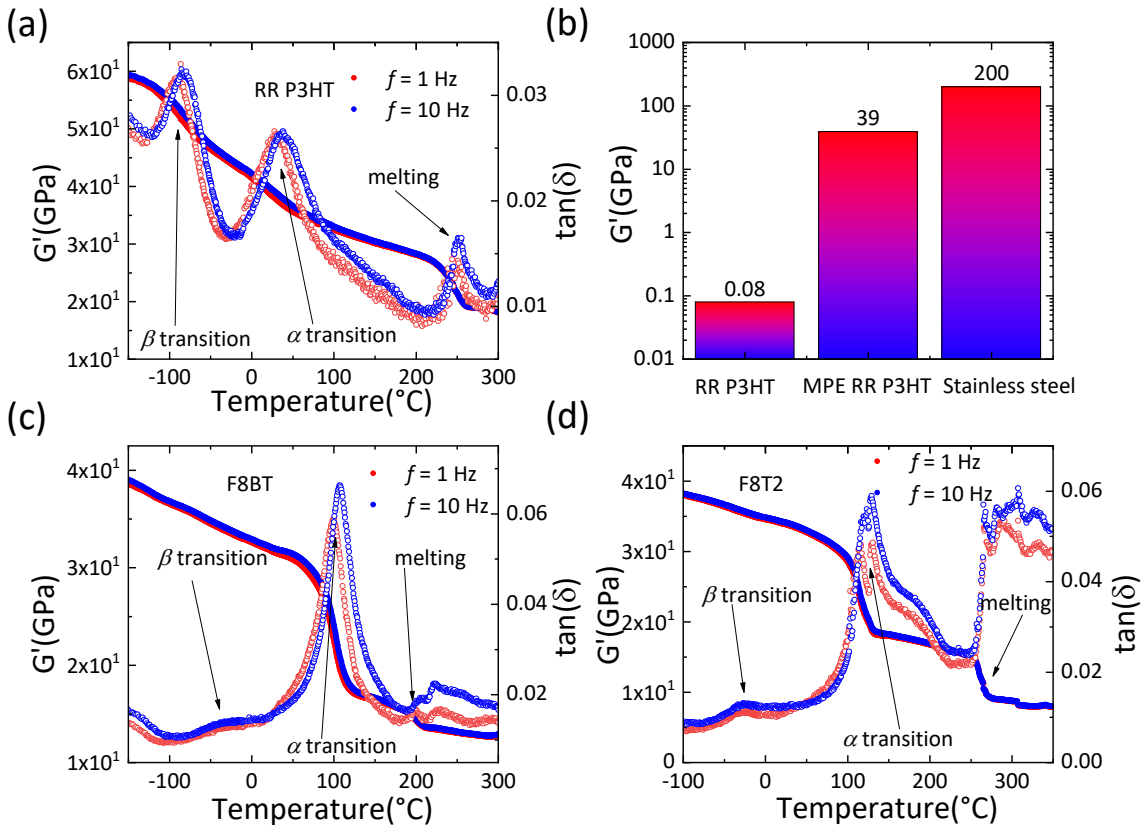

Figure 2 (a) DMA measurement results of the storage modulus G' (solid circles) and the damping factor tan (δ) (open circles) of the MPE RR P3HT sample. (b) room temperature storage modulus comparison between the pure RR P3HT powder, the MPE RR P3HT sample, and the pure stainless steel. (c) DMA measurement results of the storage modulus G' (solid circles) and the damping factor tan (δ) (open circles) of the MPE F8BT sample. (d) DMA measurement results of the storage modulus G' (solid circles) and the damping factor tan (δ) (open circles) of the MPE F8T2 sample. (Absolute values for G' are of limited accuracy due to the sample geometry, or something to this effect).

Table 1 Summary of the effective mobility value ζ, predicted backbone T_g by Equation (1), experimentally measured backbone T_g with oscillatory shear rheometry in ref. [51], and experimentally measured backbone T_g with the DMA technique in this work.

Polymer	ζ	Pred. T_g (℃)	Exp. T_g (℃) oscillatory shear rheometry	Exp. T_g (℃) DMA (1 Hz)
P3HT	0.873	18 [51]	14 [51]	28
F8BT	0.795	103 [51]	112 [51]	100
F8T2	0.805	92 [51]	102 [51]	113

We studied a family of near-amorphous D-A polymers with fused/extended donor units. The parent polymer, C_{16} IDT-BT, is a high mobility model system with a nearly amorphous microstructure and only a very limited degree of crystallinity observable in grazing incidence X-ray diffraction[67]. The favorable intramolecular interaction between the hydrogen atom of the IDT unit and the neighboring nitrogen atom of the BT unit planarizes the backbone by

introducing a steep torsion potential at the linkage [68]. These features contribute to the built-in resilience of the polymer electronic structure to structural disorder, and imparts significant backbone rigidity with a highly planar backbone structure, demonstrating very small energetic disorder and high-mobility charge transport properties[24]. The C_{16} alkyl chains attached to the sp^3 carbon atom within the IDT unit introduce significant steric hindrance between chains, largely disrupting long-range interchain π-stacking and also provide the material with high solubility in a wide range of organic solvents [24]. The microstructural properties were investigated extensively in previous work and are not reproduced here[67]. The near-amorphous microstructure of IDT-BT compared with semicrystalline polymers makes it an ideal system for experimental observation of the glass transition process using DMA [69]. Like for P3HT the storage modulus (solid circles) and damping factor (open circles) of the MPE C_{16} IDT-BT were measured with two oscillating frequencies of 1 Hz and 10 Hz separately. Three distinct transitions manifesting themselves as peaks of the damping factor within the temperature range between -100 °C and 300 °C (Figure 3(a)): A first transition is observed at -27 °C at 1Hz and at a higher temperature of -19 °C for the faster, 10Hz modulation frequency. We interpret this as the β-transition associated with the side chain relaxation process. The second transition at 56°C (77°C) for the 1(10) Hz modulation is interpreted as the α-transition/glass transition associated with the backbone relaxation. The melting transition is observed at 278 °C and is independent of modulation frequency.

In a recent study, pseudo free-standing, film-on-water tensile measurements show the high storage modulus (0.75 GPa, Figure 3(b)) of C_{16} IDT-BT, which is triple the value of more crystalline polymers such as DPP-TT [43] , and is almost one order of magnitude higher than the value of RR P3HT[60] (0.08 GPa, Figure 2(b)), which was ascribed to the torsion-free, highly rigid backbone of C_{16} IDT-BT [43]. With the consideration of the modest T_g < 60 °C, C_{16} IDT-BT reveals unique mechanical characteristics compared with other semiconducting polymers, namely, the high storage modulus does not necessarily transfer into a high T_g or sacrifice mechanical deformability of materials [43]. This may also suggest that the modest T_g < 60 °C at 1Hz may be a manifestation of a relatively large free volume facilitating easy backbone dynamics within the amorphous regions rather than of any intrachain structural relaxations such as the rotation of donor or acceptor units around the single bond linkages. Like for RR P3HT the storage modulus for the MPE samples is in between the value of pure IDT-BT polymers [43] and the value of stainless steel [61] (Figure 3(b)).

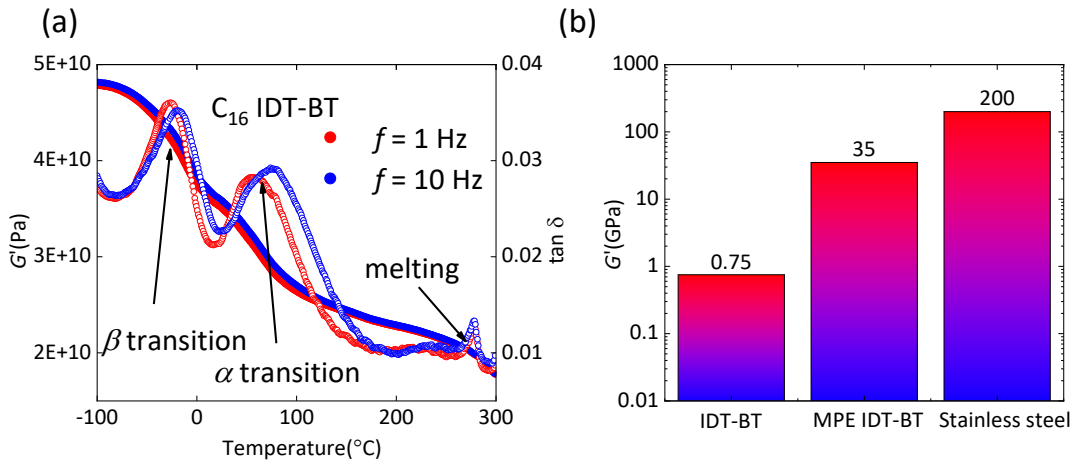

Figure 3 (a) DMA measurements of the storage modulus G'(solid circles) and the damping factor tan (δ) (open circles) for of C_{16} IDT-BT MPE samples (b) room temperature storage modulus comparison between pure C_{16} IDT-BT powder, C_{16} IDT-BT MPE sample and pure stainless steel (used for making the material pockets). Reproduced with permission [43] (Absolute values for G' are of limited accuracy due to the sample geometry, or something to this effect).

Expanding on the design motif of C_{16} IDT-BT, a series of structurally similar near-amorphous D-A copolymers were also investigated. These polymers exhibit further extended and rigidified donor units, including naphthacenodithiophene (NDT)[70], thienobenzo [b]indacenodithiophene (TBIDT)[71], and dithiopheneindenofluorene (TIF)[72]. The underlying electronic design motive for these polymers is to facilitate polaron delocalization along the extended backbone and thus, further improve on the overall charge transport properties. Figure 4 compares the four polymers in terms of charge transport, photophysical, and mechanical properties. From the saturation transfer curves and saturation mobility summarized in Figure 4 (a) and Table 2, it is clear that within this family of polymers the donor unit extension strategy does not in all cases improve source/drain current and field-effect mobility. The strategy works for C_{16} TIF-BT, which exhibits a higher current and field-effect mobility than C_{16} IDT-BT, but it fails for TBIDT-BT and NDT-BT, which disappointingly exhibit lower mobilities than C_{16} IDT-BT.

Interestingly, these derivatives exhibit significant differences not only in their charge transport properties, but also in terms of their energetic disorder[71] and luminescence properties [31], which has been correlated with molecular-level microstructure differences[71][72]. The presence of close interchain interactions has been found to be crucial for achieving high carrier mobilities in these systems[31]. Due to the lack of long-range order within these near-amorphous materials, interchain short contacts between neighboring donor/acceptor segments are required for facilitating interchain charge hopping steps, which can be considered bottlenecks for charge

transport over mesoscopic length scales. From the optical point of view these short contact regions have also been shown to be associated with a special pinned internal charge transfer (pICT) state[31], which are on-chain excitations that are stabilized by the presence of a close-packing and crossing adjacent chain. These excitations cause sub-bandgap absorption features predicted by quantum-chemical (INDO/SCI) excited-state calculation and are experimentally confirmed from photothermal deflection spectroscopy (PDS) measurements as sub-bandgap shoulders [31]. The degree of interchain overlapping around short contacts is well correlated with the radiative decay rate (k_r) of the pICT state.

Herein we combine PDS measurements and mechanical property characterization with results from DMA, to better understand the microstructure characteristics that underpin the charge transport properties for these promising near-amorphous D-A polymers. Given that these interchain short contacts are likely to confer the majority part of the microscopic interchain “frictional" forces within solid-state polymer films, it is desirable to probe these frictional forces directly with mechanical techniques. DMA measurements were performed on this series of polymers to investigate whether there is a correlation between the degrees of interchain interactions as measured by the strength of sub-bandgap absorption transitions in PDS spectra and the glass-transition temperature of these polymers. Such a link might be expected because the main-chain cooperative motion[73] occurring above the glass transition requires enough thermal energy to break these interchain contacts. Hence, we expect a trend for polymers with the strongest interchain contacts and strongest sub-bandgap absorption shoulder in PDS to exhibit the highest glass-transition temperature. From the PDS measurement (Figure 4c), it can be seen that C_{16} TIF-BT exhibits a broad band of sub-bandgap absorptions, while for C_{16} IDT-BT no such sub-bandgap shoulder is observed. C_{16} NDT-BT and C_{16} TBIDT-BT show sub-bandgap shoulders similar in magnitude to that of C_{16} TIF-BT, but distributed over a narrower energy range around 1.5eV and 1.7 eV, respectively. We may crudely quantify the strength of interchain contacts by integrating the sub-bandgap absorption coefficient over these shoulders and this reveals an empirical correlation with the measured T_g values (Table 2). The detailed procedure for these calculations can be found within the experimental section. Interestingly, the DMA measurements exhibit a trend within the family of IDT-BT derivatives. While the β transition happens at roughly the same temperature around -20 °C due to the same C_{16} alkyl side chains of these four polymers, there exists a significant difference in terms of the glass transition and melting process. For the glass transition temperature, a clear trend of C_{16} IDT-BT< C_{16} TBIDT-BT < C_{16} NDT-BT <C_{16} TIF-BT is

observed, with C_{16} TIF-BT exhibiting the highest T_g = 141 °C (Figure 4 (b), Table 2). Using Gomez's model, theoretical T_g values of these four polymers are calculated, which are all significantly lower than the experimental values measured from DMA, likely to reflect the effect of backbone rigidity to increase T_g. Interestingly, the trend of T_g agrees well with the trend of sub-bandgap absorption coefficient area, which suggests that there may be a correlation between the strength of interchain contacts and the T_g. In the supplementary information, we further compare the storage modulus and damping factor of the MPE samples of these four materials in detail (Figure S1).

Of course, it is not possible to unambiguously attribute this increase in T_g to stronger interchain interactions alone, as also the differences in backbone design and chain rigidity[74], molecular weight and side chain density (we kept side chain length the same throughout this series) may exert a significant influence. Backbone rigidity is likely to be an important factor, as all the polymers with an extended donor unit have higher T_g than C_{16} IDT-BT. The interpretation is further complicated by the length of the donor unit influencing both single-chain rigidity but potentially also facilitating closer interchain packing owing to a reduced side chain density. However, we find it remarkable that C_{16} TIF-BT, whose donor block length and side chain density is intermediate between those of C_{16} IDT-BT and C_{16} TBIDT-BT, has in fact the highest T_g and the highest density of interchain close contact points, as judged from the PDS spectra. This suggests that these close contact points are in fact a contributing factor in governing T_g, and thus, a high T_g could be a fingerprint of the close interchain interactions that are needed to achieve high carrier mobilities in these systems. A high T_g is also of course desirable for other reasons, for example, to ensure stability when devices are operated or stored at elevated temperatures.

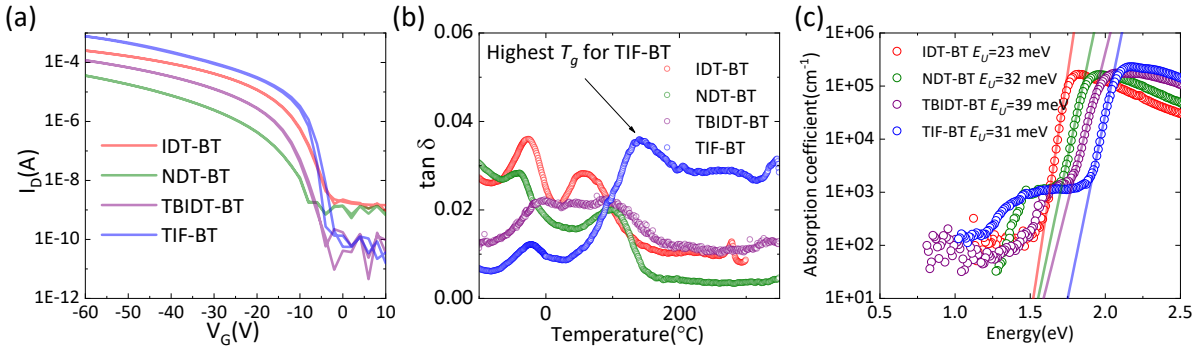

Figure 4 (a) saturation transfer curves for top-gate-bottom-contact OFETs (L = 20 µm, W = 1mm) with spin-coated C_{16} IDT-BT, C_{16} NDT-BT, C_{16} TBIDT-BT, and C_{16} TIF-BT as active layer and 480 *nm* Cytop as dielectric layer. Reproduced with permission[68][70] (b) DMA measurement results (oscillating frequency of 1 Hz) on MPE samples of C_{16} IDT-BT, C_{16} NDT-BT, C_{16} TBIDT-BT, and C_{16} TIF-BT

materials. (c) PDS spectra of spin-coated C_{16} IDT-BT, C_{16} NDT-BT, C_{16} TBIDT-BT, and C_{16} TIF-BT thin-film samples. Reproduced with permission[68][70].

Table 2 Summary of the properties of the near-amorphous D-A polymers

Polymer	ζ	Pred. T_g (℃)	Exp. T_g (℃) DMA (1 Hz) T_g (°C)	$S_{sub\text{-}bandgap}$	E_U (meV)	μ_{sat} ($cm^2V^{-1}s^{-1}$)
IDT-BT	0.91	-24	56	NA	23	1
NDT-BT	0.86	31	101	33057	32	0.4
TBIDT-BT	0.88	9	91	28084	39	0.8
TIF-BT	0.885	4	141	64737	31	3

Finally, we further extend the DMA measurements to three semi-crystalline D-A copolymers and one recently developed naphthalene-co-naphthalene (NN) fused polymer [75][76], which is an unusual conjugated polymer as it does not contain any single bonds along its backbone. All four polymers exhibit higher crystallinity than found in the C_{16} IDT-BT family. The chemical structures of these four polymers are shown in Figure 1 (c), including two widely studied, high mobility ambipolar diketopyrrolopyrrole (DPP) copolymers, namely DPP-BTz[77] and DPP-DTT[78], together with the benchmark n-type polymer P(NDI2OD-T2)[79]. The polymers have outstanding p-type mobility of 1-3 cm^2 $V^{-1}s^{-1}$ (DPP-BTz, DPP-DTT) and n-type mobility of 0.1-1 $cm^2/V^{-1}s^{-1}$ (P(NDI2OD-T2), NN fused polymer). Significant differences are observed in the DMA measurements of these semi-crystalline materials compared with the near-amorphous C_{16} IDT-BT family. For all these four semicrystalline polymers, there is only one prominent peak in the tan (δ), all located below 0 °C, which should be the β-transition related with the relaxation of side chains, while it is difficult to probe the α-transition unambiguously due to the much lower signal strength compared with the β-transition. This is likely due to the smaller amorphous content of these highly-crystalline materials compared with near-amorphous polymers like C_{16} IDT-BT, leading to smaller amounts of material responding with glass transition behavior and hence much weaker signals, as analysed quantitatively in previous work [69].

For the DPP-BTz polymer, besides the clear β-transition at -50 °C, there is a small peak around 65 °C, which is possibly the backbone glass transition peak, since a noticeable shoulder appears concurrently within the storage modulus, as shown in Figure 5 (a). However, there is some doubt about this interpretation, since we are not able to observe the frequency-dependence of

this transition, which may be obscured by the weak and broad signals around the potential transition temperature. In DPP-DTT a clear β-transition at -65 °C is observed, which is also confirmed from the drop of *G'* around the range of the transition temperature. However, it is again not easy to locate the temperature of the α-transition. There are two possible temperature regimes that may be related to the α-transition, herein highlighted with vertical dotted lines with the numbering on the side in Figure 5 (b). The first potential transition appears as the shoulder of the β-transition at -16 °C, while for the second potential transition it appears as a broad peak around 175 °C. Since we are not able to observe the clear drop of *G'* during these two potential transitions, we cannot claim these as unambiguous backbone glass transitions of DPP-DTT. For the polymer P (NDI2OD-T2), well-resolved β-transition (-25 °C) and melting peak (295 °C) exist, which is shown in Figure 5 (c), however, it is again difficult to locate the α-transition of this polymer unambiguously, we only observe a broad and weak peak around 200-220 °C. Interestingly, our DMA results agree quantitatively well with a recent work characterize the same polymer with the DMA technique using a woven glass-mesh [57] to reinforce polymer powder rather than the steel material pocket used in this work. Finally, for the DMA results of NN fused polymer presented in Figure 5 (d), the β-transition (-25 °C) is well-resolved at a peak of the tan (δ), also a certain degree of skewness exist for this peak, which may imply the potential existence of another α-transition peak with smaller amplitude at a higher temperature. In Table 3, we summarise the theoretical mobility and backbone T_g, as a reference to our experimental results. It is not possible to confirm or refute the applicability of the theoretical glass transition model to these semicrystalline polymers based on our data.

Table 3 Summary of the effective mobility value ζ, predicted backbone T_g by Equation (1)

Polymer	ζ	Pred. T_g (℃)
DPP-BTz	0.895	-7
DPP-DTT	0.89	0
P(NDI2OD-T2)	0.846	47
NN fused polymer	0.856	36

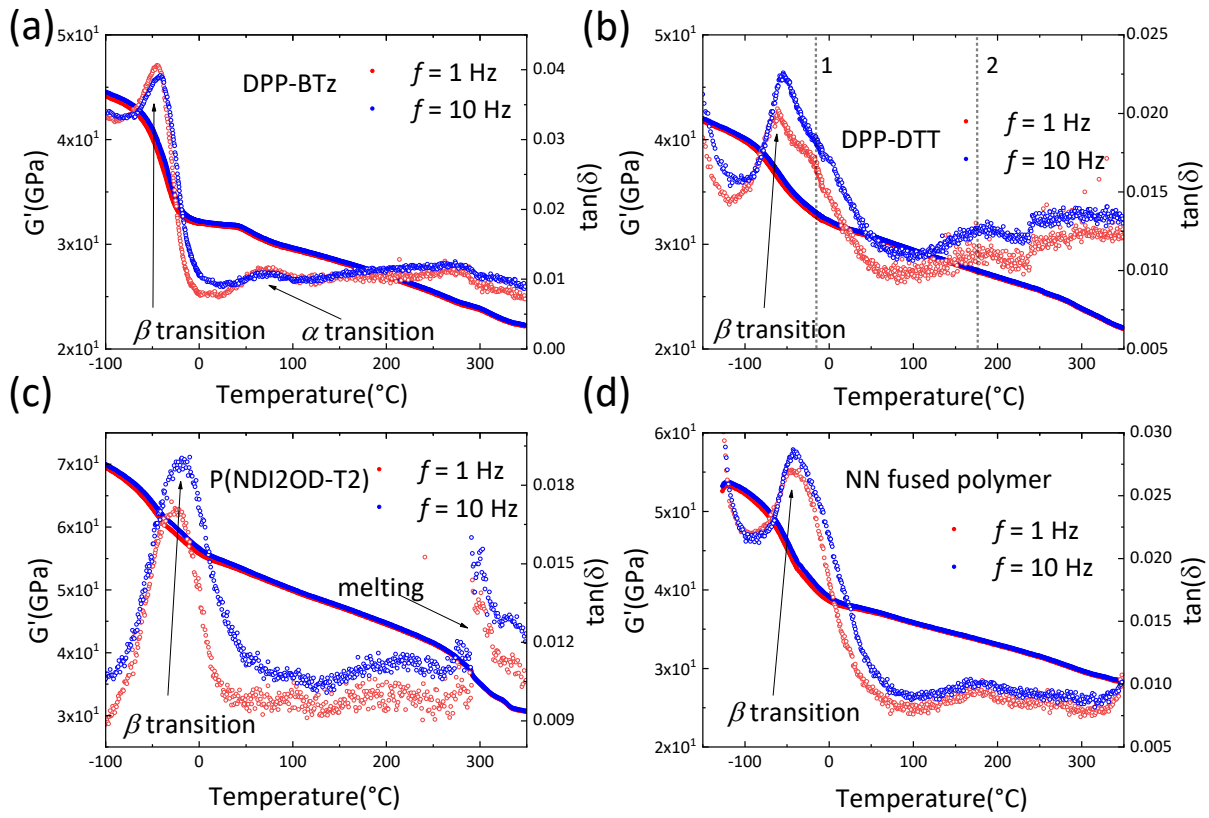

Figure 5 DMA measurement results of the storage modulus *G'* (solid circles) and the damping factor tan (δ) (open circles) of (a) MPE DPP-BTz sample, (b) MPE DPP-DTT sample, (c) MPE P(NDI2OD-T2)sample, and (d) MPE NN fused polymer sample. (Absolute values for G' are of limited accuracy due to the sample geometry, or something to this effect).

Conclusion

In this work, we have measured T_g's for a range of conjugated polymers whose mechanical properties had hitherto not been investigated yet and which are important and widely studied polymers for applications in OFETs. For the three traditional polyalkylthiophene and polydialkylfluorene polymers, our DMA results agree well with the values predicted by a theoretical model proposed recently, fully confirming the accuracy of our DMA measurements. We also characterised a class of near-amorphous polymers based on IDT-BT, which show significantly higher T_g's than the theoretically predicted values. We observed an empirical correlation between the T_g and the strength of interchain short contacts as manifesting themselves in sub-bandgap optical absorption and charge carrier mobilities. Stronger interchain short-contacts and higher mobilities appear correlated with higher T_g. The T_g values in this family of polymers is significantly higher than what is theoretically predicted which maybe a manifestation of the potential impact of the fused/extended backbone structure which is not

considered in the model. Finally, for a range of semi-crystalline copolymers, we are not able to probe T_gs unambiguously likely due to the low portion of amorphous domains responding to the measurements. Our study demonstrates the importance of studying the mechanical properties and T_g of conjugated polymers for gaining additional insights into photophysical and charge transport properties. The DMA technique is an easily accessible benchtop technique with excellent sensitivity that is applicable to a wide range of amorphous and semi-crystalline conjugated polymers for different optoelectronic applications. The use of versatile operation modes combined with setups of higher sensitivity could offer the detection of more subtle glass transition signals, thereby providing essential thermodynamic properties for other state-of-the-art semi-crystalline polymers as well.

Acknowledgements:

We gratefully acknowledge financial support by the Engineering and Physical Sciences Research Council (EPSRC) through a programme grant (EP/M005143/1) and by the European Research Council (ERC) through a Synergy grant (SC2 610115).

Experimental Section

DMA measurements: A Triton 2000 DMA, in combination with a material pocket accessory, was used to conduct all DMA measurements shown in the work. 7.5 mg polymers powder were enveloped within the metal pocket and mounted in the DMA. Single cantilever bending mode was chosen as the deformation mode. Displacement was set as 0.05 mm; compared with the 10 mm length sample dimension it was well within the linear viscoelastic response (LVR) region[80], within which the resultant stress responds linearly to the applied strain, and deformation of sample could completely recover after the removal of the applied strain without damage of sample to any extent. Two frequencies of 1 Hz and 10 Hz were set for the temperature sweep mode measurement, with a ramp rate set up to 4 °C/min, from -100 °C to 350 °C. Within this temperature regime, β, α, and melting processes happen sequentially during temperature increase. The highly localised and subtle structural relaxations occurring during the γ transition happens at even lower temperature than the β transition and are not within the temperature range of our experiments. During experiments, a sinusoidal strain within the linear viscoelastic region (LVR) is applied to the sample clamped through the periodic movements

of the driveshaft, whilst measuring the mechanical response (resulting stress) as a function of both oscillatory frequency and temperature. Within the LVR region, relatively small strain amplitude is applied, hence the sample would not be destroyed during experiments. Recently, this technique demonstrates its capacity for broader applications such as measuring powdered materials with pharmaceutical and biomedical significance with the help of material pocket accessory (folded sheets of stainless steel)[69]. Material pockets envelop and reinforce the polymer in order to measure these powdered materials with DMA. During measurements, polymer powders are sheared periodically within the material pockets. Hence to a certain extent, DMA measures the response of polymer powders under interchain friction directly. However, due to the unclear sample geometry, the accurate modulus of the materials could not be measured directly, which is a drawback of the material pocket approach. In other words, the much stiffer and heavier stainless steel pockets (750mg for each) would dominate modulus signal, masking the much weaker signals from lighter (7.5 mg powder used each time) and softer polymer powders. However, the temperature at which a specific relaxation happens would still induce a detectable peak in the "joint" damping factor or loss modulus of the material pocket enveloped sample (MPE sample), due to the ultra-sensitivity intrinsic to the setup's working mechanism. Since stainless steel has no structure relaxation within the measured temperature regime (-100 to 350 °C within this work) [69] , the mentioned features could be unambiguously correlated with specific relaxation processes of the target polymer enveloped. Hence only the trend of the modulus, such as turning points (kinks) in the curves could be related with the change of polymers' mechanical property at relaxation rather than the absolute value of modulus, which is dominated by stiffer and heavier material pockets. However, the peaks of these damping factors have accurate physical interpretations as we discussed above, and the position of these peaks could be related to the temperatures at which certain relaxation processes in the polymer happen.

Photothermal Deflection Spectroscopy (PDS): Polymer samples were spin-coated on infrared transparent fused silica substrates (Quartz Windows from the UQG Optics) and were subsequently annealed with the same condition as for OFET fabrication. A home built PDS setup was used to measure sub-bandgap absorption spectra. PDS technique is a pump-probe spectroscopy technique in general, capable of probing orders of magnitude lower absorption compared with traditional UV-Vis absorption technique due to its unique working mechanism [81]. Simply put, the heat released by the absorption of the monochromatic light (directed perpendicular onto the sample, pump light) deflects the probing laser beam grazing the sample

surface, the extent of which is recorded by the following position detector and translated into absorbance at each specific wavelength.

OFETs fabrication: Top-gate-bottom-contact OFETs are fabricated to investigate charge transport properties of related materials. Photolithographically defined interdigitated electrodes (3 nm chromium as the first adhesion layer with 15nm gold layer on top) are fabricated first on top of glass substrates (20 μm channel length and 1000 μm channel width). After this conjugated polymers and Cytop layers are deposited and annealed sequentially following the same recipe in ref. [56] . As the final step, gate electrodes are evaporated through the shadow mask to complete device fabrications.

OFET testing: OFETs are measured at room temperature in a controlled nitrogen environment with oxygen and moisture level below 5 ppm, with an Agilent 4155B Semiconductor Parameter Analyzer to take transfer and output characteristics of devices from three Source Measure Units attached to the source, drain and gate electrodes.

Calculation of the sub-bandgap area of the PDS measurements:

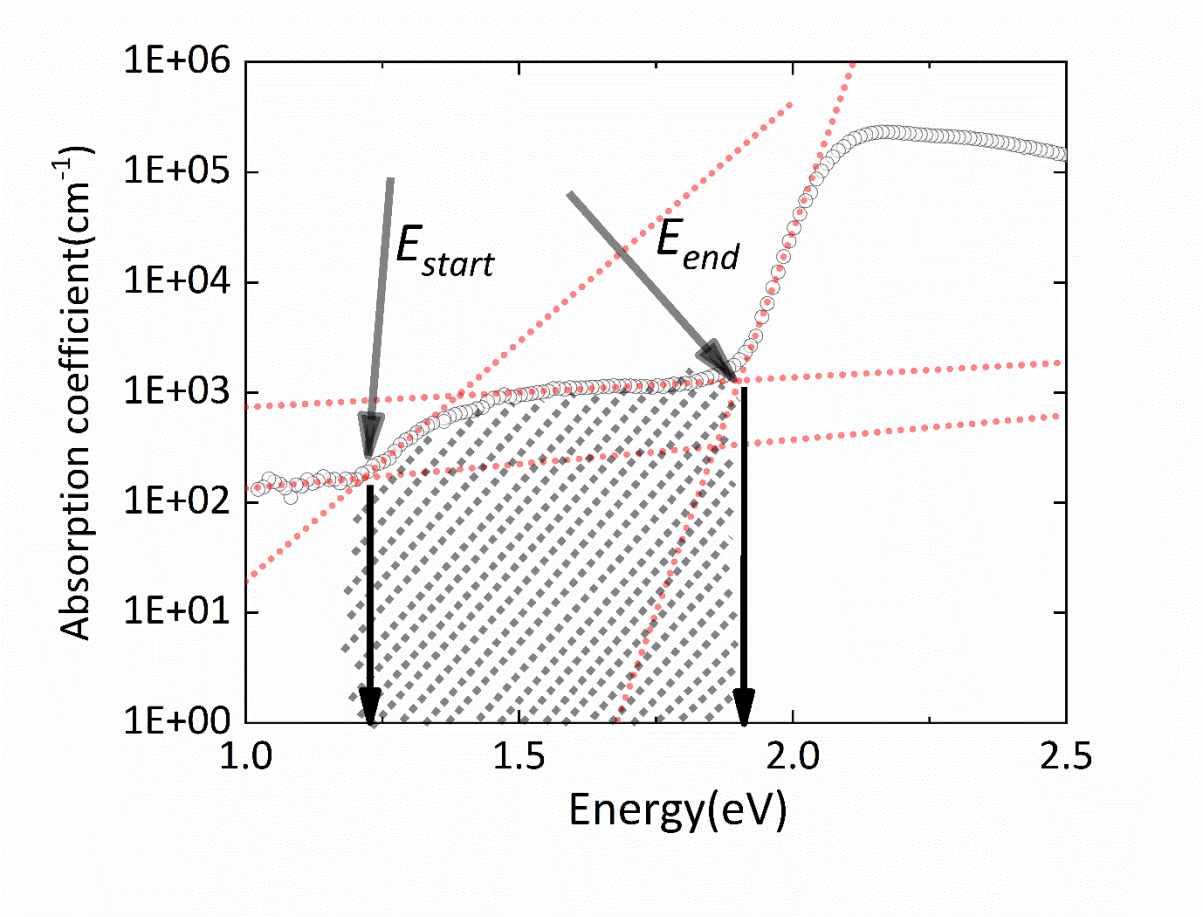

The starting and ending points of the sub-bandgap shoulder area are identified through the intersection points of absorption spectrum fitting of adjacent regions, namely the E_{start} and the E_{end} within the plots. All the Y axis values (absorption coefficients) within this region are summed up, representing the area of sub-bandgap in Table 2.

Reference

[1] H. Sirringhaus, *Adv. Mater.* **2014**, *26*, 1319.

[2] X. Gu, L. Shaw, K. Gu, M. F. Toney, Z. Bao, *Nat. Commun.* **2018**, *9*, 534.

[3] J. Zaumseil, R. H. Friend, H. Sirringhaus, *Nat. Mater.* **2006**, *5*, 69.

[4] C. Cea, G. D. Spyropoulos, P. Jastrzebska-Perfect, J. J. Ferrero, J. N. Gelinas, D. Khodagholy, *Nat. Mater.* **2020**, *19*, 679.

[5] Y. Shi, L. Jiang, J. Liu, Z. Tu, Y. Hu, Q. Wu, Y. Yi, E. Gann, C. R. McNeill, H. Li, W. Hu, D. Zhu, H. Sirringhaus, *Nat. Commun.* **2018**, *9*, 2933.

[6] D. Ohayon, G. Nikiforidis, A. Savva, A. Giugni, S. Wustoni, T. Palanisamy, X. Chen, I. P. Maria, E. Di Fabrizio, P. M. F. J. Costa, I. McCulloch, S. Inal, *Nat. Mater.* **2020**, *19*, 456.

[7] S. Inal, J. Rivnay, A.-O. Suiu, G. G. Malliaras, I. McCulloch, *Acc. Chem. Res.* **2018**, *51*, 1368.

[8] J. Wang, D. Ye, Q. Meng, C. an Di, D. Zhu, *Adv. Mater. Technol.* **2020**, *5*, 1.

[9] H. Zhu, E. Shin, A. Liu, D. Ji, Y. Xu, Y. Noh, *Adv. Funct. Mater.* **2020**, *30*, 1904588.

[10] G. Schwartz, B. C.-K. Tee, J. Mei, A. L. Appleton, D. H. Kim, H. Wang, Z. Bao, *Nat. Commun.* **2013**, *4*, 1859.

[11] C. Liu, T. Minari, X. Lu, A. Kumatani, K. Takimiya, K. Tsukagoshi, *Adv. Mater.* **2011**, *23*, 523.

[12] X. Guo, A. Facchetti, *Nat. Mater.* **2020**, *19*, 922.

[13] C. Wang, H. Dong, W. Hu, Y. Liu, D. Zhu, *Chem. Rev.* **2012**, *112*, 2208.

[14] X. Guo, N. Zhou, S. J. Lou, J. Smith, D. B. Tice, J. W. Hennek, R. P. Ortiz, J. T. L. Navarrete, S. Li, J. Strzalka, L. X. Chen, R. P. H. Chang, A. Facchetti, T. J. Marks, *Nat. Photonics* **2013**, *7*, 825.

[15] D. Zhang, L. Duan, C. Li, Y. Li, H. Li, D. Zhang, Y. Qiu, *Adv. Mater.* **2014**, *26*, 5050.

[16] J. Zhang, H. S. Tan, X. Guo, A. Facchetti, H. Yan, *Nat. Energy* **2018**, *3*, 720.

[17] T. Huang, W. Jiang, L. Duan, *J. Mater. Chem. C* **2018**, *6*, 5577.

[18] Y. Li, D.-K. Lee, J. Y. Kim, B. Kim, N.-G. Park, K. Kim, J.-H. Shin, I.-S. Choi, M. J. Ko, *Energy Environ. Sci.* **2012**, *5*, 8950.

[19] H. Dong, X. Fu, J. Liu, Z. Wang, W. Hu, *Adv. Mater.* **2013**, *25*, 6158.

[20] Y. Lin, M. Wood, K. Imasato, J. J. Kuo, D. Lam, N. Mortazavi, T. Slade, S. Hodge, K. Xi, M. G. Kanatzidis, D. R. Clarke, M. C. Hersam, G. J. Snyder, *Energy Environ. Sci.* **2020**, DOI 10.1039/D0EE02490B.

[21] Y. Kim, A. Chortos, W. Xu, Y. Liu, J. Y. Oh, D. Son, J. Kang, A. M. Foudeh, C. Zhu, Y. Lee, S. Niu, J. Liu, R. Pfattner, Z. Bao, T.-W. Lee, *Science (80-.).* **2018**, *360*, 998.

[22] W. Xu, S.-Y. Min, H. Hwang, T.-W. Lee, *Sci. Adv.* **2016**, *2*, e1501326.

[23] X.-J. She, D. Gustafsson, H. Sirringhaus, *Adv. Mater.* **2017**, *29*, 1604769.

[24] D. Venkateshvaran, M. Nikolka, A. Sadhanala, V. Lemaur, M. Zelazny, M. Kepa, M. Hurhangee, A. J. Kronemeijer, V. Pecunia, I. Nasrallah, I. Romanov, K. Broch, I. McCulloch, D. Emin, Y. Olivier, J. Cornil, D. Beljonne, H. Sirringhaus, *Nature* **2014**, *515*, 384.

[25] S. Schott, U. Chopra, V. Lemaur, A. Melnyk, Y. Olivier, R. Di Pietro, I. Romanov, R. L. Carey, X. Jiao, C. Jellett, M. Little, A. Marks, C. R. McNeill, I. McCulloch, E. R. McNellis, D. Andrienko, D. Beljonne, J. Sinova, H. Sirringhaus, *Nat. Phys.* **2019**, *15*, 814.

[26] S. Fratini, M. Nikolka, A. Salleo, G. Schweicher, H. Sirringhaus, *Nat. Mater.* **2020**, *19*, 491.

[27] R. Noriega, J. Rivnay, K. Vandewal, F. P. V Koch, N. Stingelin, P. Smith, M. F. Toney, A. Salleo, *Nat. Mater.* **2013**, *12*, 1038.

[28] S. Fratini, S. Ciuchi, D. Mayou, G. T. de Laissardière, A. Troisi, *Nat. Mater.* **2017**, *16*, 998.

[29] S. P. Senanayak, A. Z. Ashar, C. Kanimozhi, S. Patil, K. S. Narayan, *Phys. Rev. B* **2015**, *91*, 115302.

[30] R. P. Fornari, A. Troisi, *Phys. Chem. Chem. Phys.* **2014**, *16*, 9997.

[31] T. H. Thomas, D. J. Harkin, A. J. Gillett, V. Lemaur, M. Nikolka, A. Sadhanala, J. M. Richter, J. Armitage, H. Chen, I. McCulloch, S. M. Menke, Y. Olivier, D. Beljonne, H. Sirringhaus, *Nat. Commun.* **2019**, *10*, 2614.

[32] J. Xu, S. Wang, G.-J. N. Wang, C. Zhu, S. Luo, L. Jin, X. Gu, S. Chen, V. R. Feig, J. W. F. To, S. Rondeau-Gagné, J. Park, B. C. Schroeder, C. Lu, J. Y. Oh, Y. Wang, Y.-H. Kim, H. Yan, R. Sinclair, D. Zhou, G. Xue, B. Murmann, C. Linder, W. Cai, J. B.-H. Tok, J. W. Chung, Z. Bao, *Science (80-.).* **2017**, *355*, 59.

[33] R. Xie, R. H. Colby, E. D. Gomez, *Adv. Electron. Mater.* **2018**, *4*, 1700356.

[34] C. R. Snyder, D. M. DeLongchamp, *Curr. Opin. Solid State Mater. Sci.* **2018**, *22*, 41.

[35] C. Müller, *Chem. Mater.* **2015**, *27*, 2740.

[36] Z. Qian, Z. Cao, L. Galuska, S. Zhang, J. Xu, X. Gu, *Macromol. Chem. Phys.* **2019**, *220*, 1900062.

[37] S. E. Root, M. A. Alkhadra, D. Rodriquez, A. D. Printz, D. J. Lipomi, *Chem. Mater.* **2017**, *29*, 2646.

[38] H. Bronstein, C. B. Nielsen, B. C. Schroeder, I. McCulloch, *Nat. Rev. Chem.* **2020**, *4*, 66.

[39] X. Gu, L. Shaw, K. Gu, M. F. Toney, Z. Bao, *Nat. Commun.* **2018**, *9*, 534.

[40] G. Strobl, *The Physics of Polymers*, *Third Revised and Expanded Edition*, Springer-Verlag, Berlin Heidelberg, **2007**.

[41] J. Heijboer, *Int. J. Polym. Mater.* **1977**, *6*, 11.

[42] B. Schartel, J. H. Wendorff, *Polymer (Guildf).* **1995**, *36*, 899.

[43] Y. Zheng, G. N. Wang, J. Kang, M. Nikolka, H. Wu, H. Tran, S. Zhang, H. Yan, H. Chen, P. Y. Yuen, J. Mun, R. H. Dauskardt, I. McCulloch, J. B. -H. Tok, X. Gu, Z. Bao, *Adv. Funct. Mater.* **2019**, *1905340*, 1905340.

[44] D. Leman, M. A. Kelly, S. Ness, S. Engmann, A. Herzing, C. Snyder, H. W. Ro, R. J. Kline, D. M. DeLongchamp, L. J. Richter, *Macromolecules* **2015**, *48*, 383.

[45] S. Savagatrup, A. D. Printz, T. F. O'Connor, A. V. Zaretski, D. Rodriquez, E. J. Sawyer, K. M. Rajan, R. I. Acosta, S. E. Root, D. J. Lipomi, *Energy Environ. Sci.* **2015**, *8*, 55.

[46] W. R. Mateker, M. D. McGehee, *Adv. Mater.* **2017**, *29*, 1603940.

[47] A. Gumyusenge, D. T. Tran, X. Luo, G. M. Pitch, Y. Zhao, K. A. Jenkins, T. J. Dunn, A. L. Ayzner, B. M. Savoie, J. Mei, *Science (80-.).* **2018**, *362*, 1131.

[48] B. McCulloch, V. Ho, M. Hoarfrost, C. Stanley, C. Do, W. T. Heller, R. A. Segalman, *Macromolecules* **2013**, *46*, 1899.

[49] C. Müller, M. Esmaeili, C. Riekel, D. W. Breiby, O. Inganäs, *Polymer (Guildf).* **2013**, *54*, 805.

[50] R. Kroon, *Synthesis & Properties of Pi-Conjugated Polymers for OPV*, **2013**.

[51] R. Xie, A. R. Weisen, Y. Lee, M. A. Aplan, A. M. Fenton, A. E. Masucci, F. Kempe, M. Sommer, C. W. Pester, R. H. Colby, E. D. Gomez, *Nat. Commun.* **2020**, *11*, 893.

[52] A. K. Sircar, M. L. Galaska, S. Rodrigues, R. P. Chartoff, *Rubber Chem. Technol.* **1999**, *72*, 513.

[53] Z. Qian, L. Galuska, W. W. McNutt, M. U. Ocheje, Y. He, Z. Cao, S. Zhang, J. Xu, K. Hong, R. B. Goodman, S. Rondeau-Gagné, J. Mei, X. Gu, *J. Polym. Sci. Part B Polym. Phys.* **2019**, *57*, 1635.

[54] D. S. Jones, Y. Tian, O. Abu-Diak, G. P. Andrews, *Adv. Drug Deliv. Rev.* **2012**, *64*, 440.

[55] M. S. Vezie, S. Few, I. Meager, G. Pieridou, B. Dörling, R. S. Ashraf, A. R. Goñi, H. Bronstein, I. McCulloch, S. C. Hayes, M. Campoy-Quiles, J. Nelson, *Nat. Mater.* **2016**, *15*, 746.

[56] M. Nikolka, I. Nasrallah, B. Rose, M. K. Ravva, K. Broch, A. Sadhanala, D. Harkin, J. Charmet, M. Hurhangee, A. Brown, S. Illig, P. Too, J. Jongman, I. McCulloch, J.-L. Bredas, H. Sirringhaus, *Nat. Mater.* **2017**, *16*, 356.

[57] A. Sharma, X. Pan, J. M. Bjuggren, D. Gedefaw, X. Xu, R. Kroon, E. Wang, J. A. Campbell, D. A. Lewis, M. R. Andersson, *Chem. Mater.* **2019**, *31*, 6740.

[58] P. E. Hopkinson, P. A. Staniec, A. J. Pearson, A. D. F. Dunbar, T. Wang, A. J. Ryan, R. A. L. Jones, D. G. Lidzey, A. M. Donald, *Macromolecules* **2011**, *44*, 2908.

[59] R. A. Talja, Y. H. Roos, *Thermochim. Acta* **2001**, *380*, 109.

[60] R. Xie, Y. Lee, M. P. Aplan, N. J. Caggiano, C. Müller, R. H. Colby, E. D. Gomez, *Macromolecules* **2017**, *50*, 5146.

[61] W. B. Choi, L. Prchlik, S. Sampath, A. Gouldstone, *J. Therm. Spray Technol.* **2009**, *18*, 58.

[62] H. Sirringhaus, P. J. Brown, R. H. Friend, M. M. Nielsen, K. Bechgaard, B. M. W. Langeveld-Voss, A. J. H. Spiering, R. A. J. Janssen, E. W. Meijer, P. Herwig, D. M. de Leeuw, *Nature* **1999**, *401*, 685.

[63] H. Tanaka, H. Kajii, Y. Ohmori, *Synth. Met.* **2015**, *203*, 10.

[64] K. Koiwai, H. Kajii, Y. Ohmori, *Synth. Met.* **2011**, *161*, 2107.

[65] M. Kim, S. U. Ryu, S. A. Park, K. Choi, T. Kim, D. Chung, T. Park, *Adv. Funct. Mater.* **2020**, *30*, 1904545.

[66] H. Sirringhaus, *Adv. Mater.* **2014**, *26*, 1319.

[67] X. Zhang, H. Bronstein, A. J. Kronemeijer, J. Smith, Y. Kim, R. J. Kline, L. J. Richter, T. D. Anthopoulos, H. Sirringhaus, K. Song, M. Heeney, W. Zhang, I. McCulloch, D. M. DeLongchamp, *Nat. Commun.* **2013**, *4*, 2238.

[68] A. Wadsworth, H. Chen, K. J. Thorley, C. Cendra, M. Nikolka, H. Bristow, M. Moser, A. Salleo, T. D. Anthopoulos, H. Sirringhaus, I. McCulloch, *J. Am. Chem. Soc.* **2020**, *142*, 652.

[69] P. G. Royall, C. Y. Huang, S. W. J. Tang, J. Duncan, G. Van-De-Velde, M. B. Brown, *Int. J. Pharm.* **2005**, *301*, 181.

[70] A.-C. Knall, R. S. Ashraf, M. Nikolka, C. B. Nielsen, B. Purushothaman, A. Sadhanala, M. Hurhangee, K. Broch, D. J. Harkin, J. Novák, M. Neophytou, P. Hayoz, H. Sirringhaus, I. McCulloch, *Adv. Funct. Mater.* **2016**, *26*, 6961.

[71] H. Chen, A. Wadsworth, C. Ma, A. Nanni, W. Zhang, M. Nikolka, A. M. T. Luci, L. M. A. Perdigão, K. J. Thorley, C. Cendra, B. Larson, G. Rumbles, T. D. Anthopoulos, A. Salleo, G. Costantini, H. Sirringhaus, I. McCulloch, *J. Am. Chem. Soc.* **2019**, *141*, 18806.

[72] H. Chen, M. Hurhangee, M. Nikolka, W. Zhang, M. Kirkus, M. Neophytou, S. J. Cryer, D. Harkin, P. Hayoz, M. Abdi-Jalebi, C. R. McNeill, H. Sirringhaus, I. McCulloch, *Adv. Mater.* **2017**, *29*, 1702523.

[73] J. A. Forrest, J. Mattsson, *Phys. Rev. E* **2000**, *61*, R53.

[74] L. A. Galuska, W. W. McNutt, Z. Qian, S. Zhang, D. W. Weller, S. Dhakal, E. R. King, S. E. Morgan, J. D. Azoulay, J. Mei, X. Gu, *Macromolecules* **2020**, *53*, 6032.

[75] A. Onwubiko, W. Yue, C. Jellett, M. Xiao, H.-Y. Chen, M. K. Ravva, D. A. Hanifi, A.-C. Knall, B. Purushothaman, M. Nikolka, J.-C. Flores, A. Salleo, J.-L. Bredas, H. Sirringhaus, P. Hayoz, I. McCulloch, *Nat. Commun.* **2018**, *9*, 416.

[76] M. Xiao, B. Kang, S. B. Lee, L. M. A. Perdigão, A. Luci, D. A. Warr, S. P. Senanayak, M. Nikolka, M. Statz, Y. Wu, A. Sadhanala, S. Schott, R. Carey, Q. Wang, M. Lee, C.

Kim, A. Onwubiko, C. Jellett, H. Liao, W. Yue, K. Cho, G. Costantini, I. McCulloch, H. Sirringhaus, *Adv. Mater.* **2020**, *32*, 2000063.

[77] M. Gruber, S. H. Jung, S. Schott, D. Venkateshvaran, A. J. Kronemeijer, J. W. Andreasen, C. R. McNeill, W. W. H. Wong, M. Shahid, M. Heeney, J. K. Lee, H. Sirringhaus, *Chem. Sci.* **2015**, *6*, 6949.

[78] Z. Wang, Z. Liu, L. Ning, M. Xiao, Y. Yi, Z. Cai, A. Sadhanala, G. Zhang, W. Chen, H. Sirringhaus, D. Zhang, *Chem. Mater.* **2018**, *30*, 3090.

[79] H. Yan, Z. Chen, Y. Zheng, C. Newman, J. R. Quinn, F. Dötz, M. Kastler, A. Facchetti, *Nature* **2009**, *457*, 679.

[80] S. Vleeshouwers, A. M. Jamieson, R. Simha, *Polym. Eng. Sci.* **1989**, *29*, 662.

[81] S. P. Senanayak, B. Yang, T. H. Thomas, N. Giesbrecht, W. Huang, E. Gann, B. Nair, K. Goedel, S. Guha, X. Moya, C. R. McNeill, P. Docampo, A. Sadhanala, R. H. Friend, H. Sirringhaus, *Sci. Adv.* **2017**, *3*, e1601935.

Supplementary Information

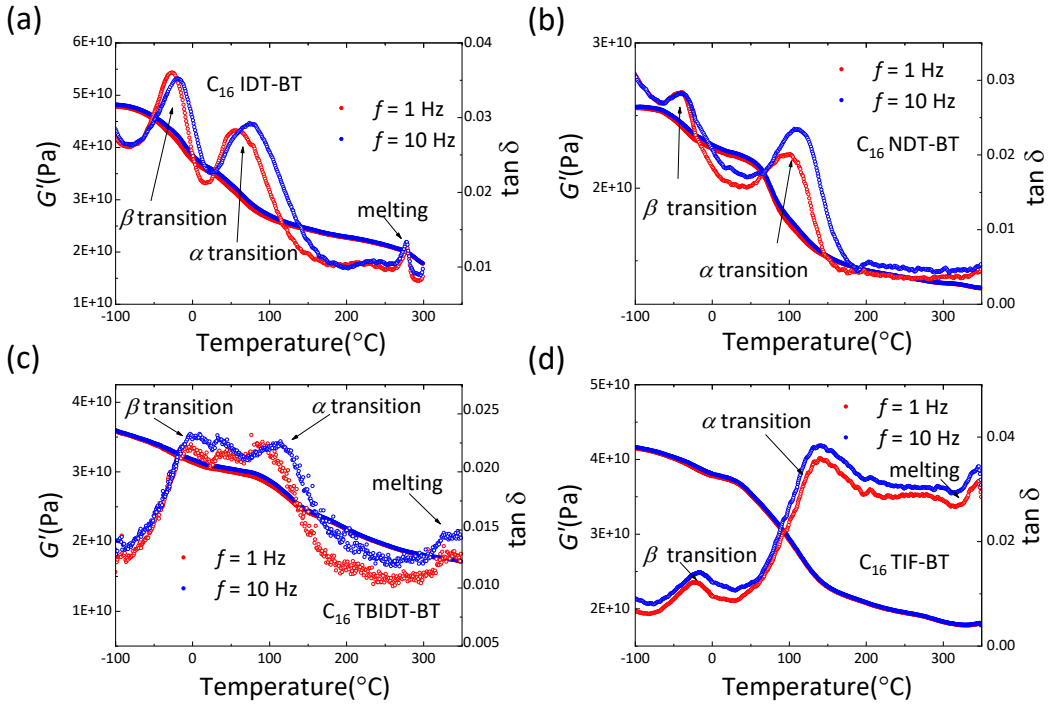

Figure S1: DMA measurement results of the storage modulus *G'* (solid circles) and the damping factor tan (δ) (open circles) of (a) MPE IDT-BT sample, (b) MPE NDT-BT sample, (c) MPE TBIDT-BT sample, and (d) MPE TIF-BT sample. (Absolute values for G' are of limited accuracy due to the sample geometry, or something to this effect).

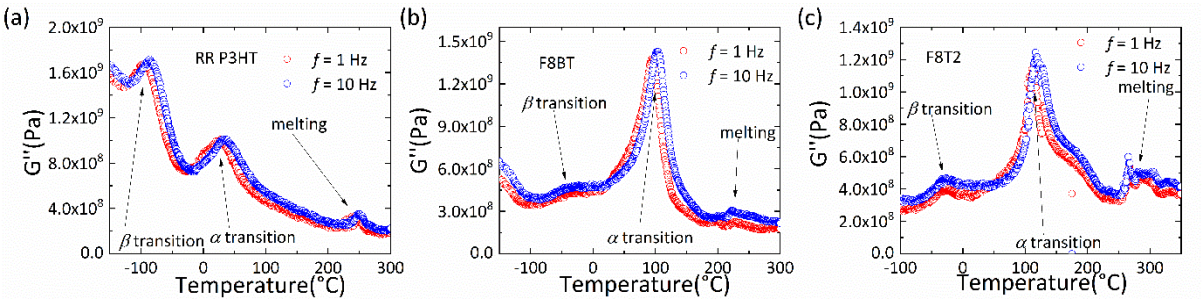

Figure S2: DMA measurement results of the loss modulus *G''* (open circles) of (a) MPE RR P3HT sample, (b) MPE F8BT sample, (c) MPE F8T2 sample (Absolute values for *G''* are of limited accuracy due to the sample geometry, or something to this effect).

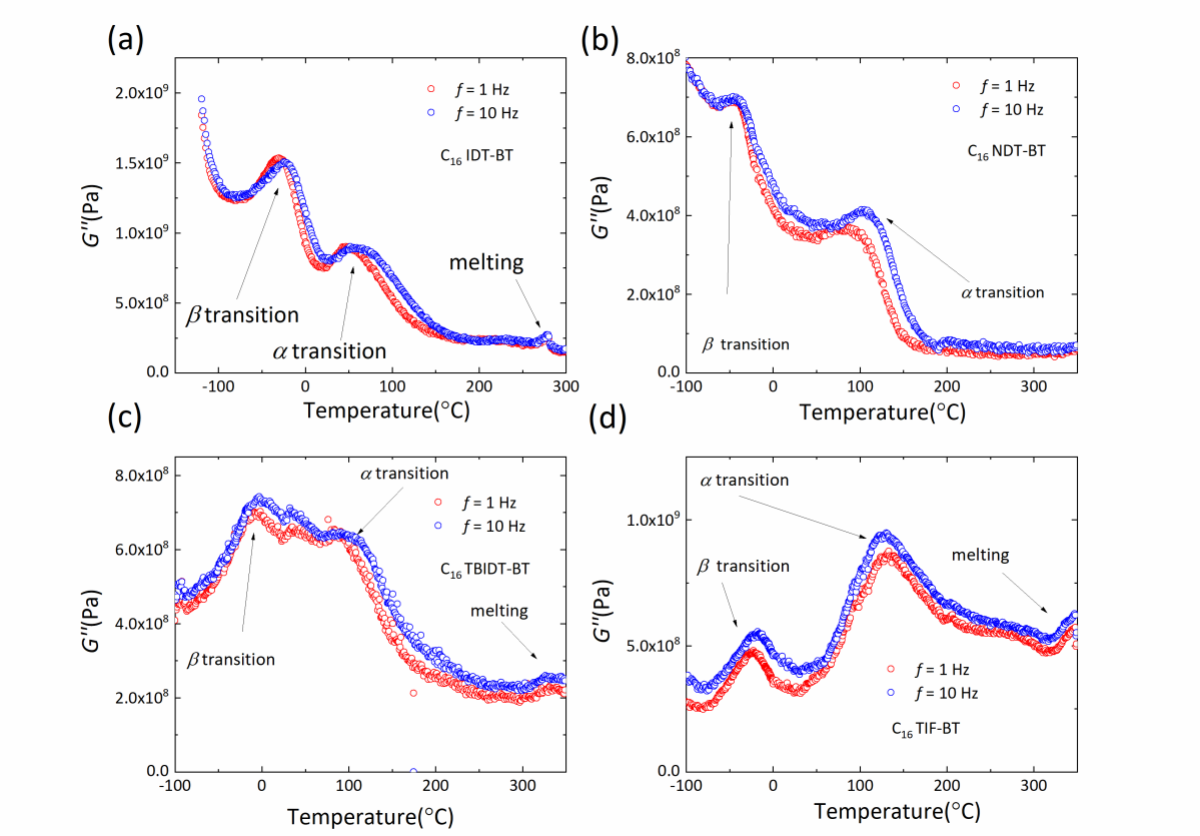

Figure S3: DMA measurement results of the loss modulus *G''* (open circles) of (a) MPE C_{16} IDT-BT sample, (b) MPE C_{16} NDT-BT sample, (c) MPE C_{16} TBIDT-BT sample, (d) MPE C_{16} TIF-BT sample (Absolute values for *G''* are of limited accuracy due to the sample geometry, or something to this effect).

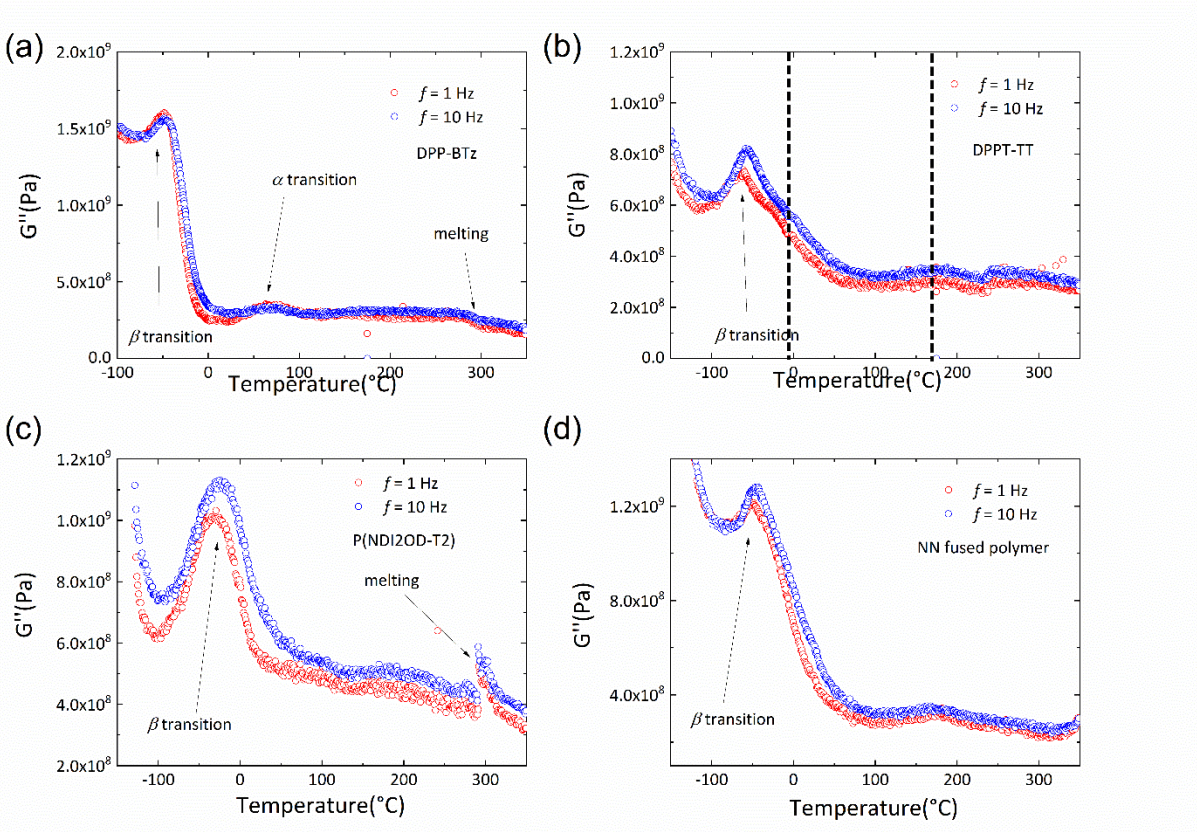

Figure S4: DMA measurement results of the loss modulus *G''* (open circles) of (a) MPE DPP-BTz sample, (b) MPE DPPT-TT sample, (c) MPE P(NDI2OD-T2) sample, (d) MPE NN fused polymer sample (Absolute values for *G''* are of limited accuracy due to the sample geometry, or something to this effect).